Applications of Holography in Fluid Mechanics and Particle Dynamics

Joseph Katz[1] and Jian Sheng[2]

[1]Department of Mechanical Engineering, The Johns Hopkins University, Baltimore, Maryland 21218-2686; email: katz@jhu.edu

[2]Aerospace Engineering and Mechanics, University of Minnesota, Minneapolis, Minnesota 55455

Annu. Rev. Fluid Mech. 2010. 42:531–55

First published online as a Review in Advance on September 21, 2009

The *Annual Review of Fluid Mechanics* is online at fluid.annualreviews.org

This article's doi:
10.1146/annurev-fluid-121108-145508

0066-4189/10/0115-0531$20.00

Key Words

holographic particle image velocimetry, digital holography, digital holographic microscopy, 3D imaging, 3D velocimetry

Abstract

The quantification of three-dimensional (3D) flow structures and particle dynamics is crucial for unveiling complex interactions in turbulent flows. This review summarizes recent advances in volumetric particle detection and 3D flow velocimetry involving holography. We introduce the fundamental principle of holography and discuss the debilitating depth-of-focus problem, along with methods that have been implemented to circumvent it. The focus of this review is on recent advances in the development of in-line digital holography in general, and digital holographic microscopy in particular. A mathematical background for the numerical reconstruction of digital holograms is followed by a summary of recently introduced 3D particle tracking and velocity measurement techniques. The review concludes with sample applications, including 3D velocity measurements that fully resolve the flow in the inner part of a turbulent boundary layer, the diffusion of oil droplets in high–Reynolds number turbulence, and predator-prey interactions among swimming microorganisms in dense suspensions, as well as oceanic and atmospheric field experiments.

1. INTRODUCTION

1.1. What Is Holography?

The idea of using wave-front reconstruction as a three-dimensional (3D) imaging technique was introduced by Gabor (1948, 1949), who also coined the term hologram. However, major advancements in holography did not occur until the introduction of the laser in the early 1960s. [Background on early work is provided by Collier et al. (1971) and Vikram (1992).] A second, recent boost to applications of holography has occurred with the introduction of digital holography, which has greatly simplified the acquisition and data-analysis procedures, but requires compromises in terms of resolution and/or the size of sample volume. In most cases, the application of holography involves two steps, namely the recording of holograms and the reconstruction of 3D images. The hologram is a record of interference between light diffracted from objects illuminated by a coherent light (the object beam) and a known reference beam. Consequently, the hologram contains information on both the phase and amplitude of the diffracted waves, which enables their reconstruction using optical or computational techniques.

There are numerous methods for recording holograms, too many to summarize in a review paper. Briefly, however, acquisition techniques are commonly characterized based on the angle between the object and reference beam. The term off-axis holography (**Figure 1*a*,*b***) refers to an optical setup in which the reference and object beams are inclined at finite angles relative to each other. Because the fringe spacing between two collimated beams is $\lambda/2 \sin(\theta/2)$, where λ is the

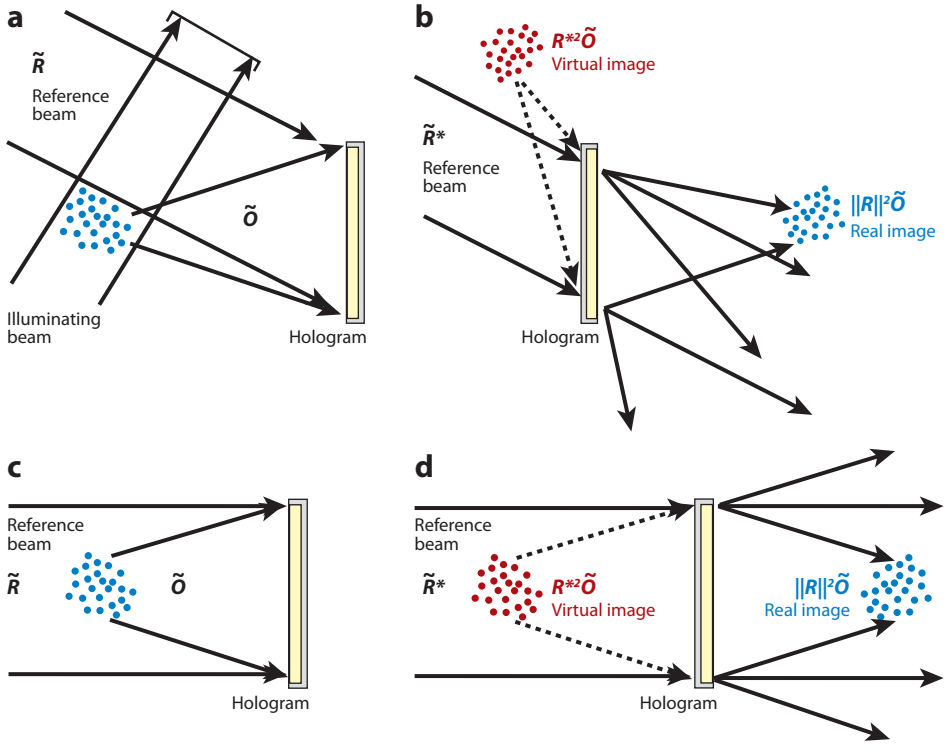

Figure 1

Principles of holography: off-axis (*a*) recording and (*b*) reconstruction, and in-line (*c*) recording and (*d*) reconstruction.

wavelength and θ is the angle between beams, the fringe spacing decreases with increasing angle, posing increasingly more stringent requirements on the recording medium. For this reason, until recently, holograms have been recorded on specialized high-resolution emulsions. The cumbersome chemical development of emulsions has led to a continued search for other media, e.g., photorefractive crystals (Gunter & Huignard 1989), film-containing bacteriorhodopsin (Barnhart et al. 2004b), and thermosensitive plates (Collier et al. 1971, Kinoshita 1992). During the optical reconstruction of holograms recorded on emulsion, they are illuminated by a laser beam aligned in the same angle as the original reference beam, but propagated in the opposite direction [a conjugate beam (**Figure 1*b***)]. The diffraction of light by the interference patterns on the film generates two 3D images, a real and a virtual one, of the objects in the original sample volume.

In in-line holography (**Figure 1*c*,*d***), the object and reference beams are parallel. In **Figure 1**, the sample volume is illuminated by a coherent wave, and light scattered from particles interferes with the undisturbed part of the wave, which serves as a reference beam. (Other in-line setups are discussed below.) The reconstruction of an in-line hologram also generates real and virtual images (**Figure 1*d***) that are located symmetrically on both sides of the film. In-line holography inherently involves a simple optical system and, due to the small angle between the interfering beams, requires a relatively low-resolution recording medium, making it particularly attractive for digital imaging. Furthermore, because of the characteristics of Mie scattering, the required laser power is minimal.

Three primary applications surfaced shortly after the invention of the laser. First, there were the detection and sizing of particles suspended in air or liquid, from aerosols to water droplets in clouds to bubbles and particles in water (Thompson 1974, Vikram 1992). Some studies involved the reconstruction of holograms, whereas others involved direct analysis based on fringe patterns in the holograms themselves. Pioneering work and early atmospheric studies were performed by Trolinger et al. (1969) and Silverman et al. (1964). In laboratories, in-line holography was used for the detection and characterization of size distributions of plankton, particles, and bubbles in water (e.g., Carder 1979, Heflinger et al. 1978, Katz 1984, Knox 1966, Knox & Brooks 1969, Stewart et al. 1973, Watson et al. 1995).

Carder et al. (1982) developed the first submersible holography system for in situ measurement of sizes and settling rates of oceanic particulates. Their sample volume was only a few cubed millimeters. Pulsed-laser holography systems were deployed by Katz et al. (1984, 1999), Malkiel et al. (1999), O'Hern et al. (1988), and Watson et al. (2001). Advancements in computing and digital imaging led to the development of automated scanning through reconstructed volumes and measurements of 3D particle distributions (Malkiel et al. 2004, 2006) in the ocean. In parallel, Milgram & Li (2002) scanned oceanic holograms and developed the procedures for numerically reconstructing them.

Second, there were measurements of surfaces of deformable bodies and, from it, the distributions of strain, stress, moments, and vibrations. In most cases, this technique involved recording off-axis hologram pairs of surfaces prior to and after deformation (Erf 1974). As video imaging was used frequently, this technique was referred to as TV holography. Finally, there was holographic interferometry of phase objects, namely measurements of changes in temperature and density in transparent media such as compressible flows based on spatial variations in refractive index (Vest 1979).

1.2. Depth-of-Focus Problem

After particle image velocimetry (PIV) appeared in the mid-1980s (Adrian 1991, Willert & Gharib 1991), the next step was to implement holographic particle image velocimetry (HPIV) as a 3D

velocity measurement technique. However, a key limitation surfaced, the so-called depth-of-focus (DOF) problem. Similar to any imaging system, the finite aperture of the hologram both limits the resolution of a reconstructed image and extends the depth over which the image remains nearly in focus (Vikram 1992). By calculating the diffraction pattern generated by a point source, one can demonstrate that the resolution is equal to $1.22\lambda(2z/d)$, where z is the distance between the hologram and in-focus plane of the particle, and d is its diameter. The corresponding DOF is proportional to d^2/λ, where the constant of proportionality depends on the intensity threshold defining the boundary of an image. For $d/\lambda \sim 40$ (20-μm particle and green light), the DOF is approximately 1 mm. Consequently, one can accurately detect a particle's coordinates that are perpendicular to the optical axis of the reference beam, but the detection of the axial location is much less accurate. The following approaches have been implemented in emulsion-based holography to alleviate this problem.

The first method has been to illuminate the flow field with a single or multiple parallel light sheets and record a single hologram. This procedure resolved the approximate axial positioning problem of the particle, but does not allow measurement of axial velocity (e.g., Konrath et al. 2002, Lozano et al. 1999). To measure all three velocity components in a fluid plane, Lobera et al. (2004) combined two interferometric reconstruction processes for a single-plane double-exposure off-axis hologram. The first process involved illumination of the entire hologram, scanning of the real image plane with a small aperture, and examining the resulting far-field fringe pattern to obtain velocity components that were parallel to the plane of the hologram. The second reconstruction involved illumination of part of the hologram with a scanning thin laser beam, which provided the velocity in a plane that included the missing component. Although not related to DOF, Fabry (1998) introduced an interesting setup consisting of an axial subject light sheet that overexposed a thin section of the emulsion, but not other areas, which recorded the interference of light scattered from particles with a separated reference beam.

The second procedure is to record off-axis holograms with large angles between the beam illuminating the sample volume and the recorded scattered light, as increasing the angle presumably reduces the DOF. Meng and colleagues (Pu & Meng 2000, 2005; Pu et al. 2000) used a 90° scattering angle and different reference beam angles for the two exposures to deal with directional ambiguity (**Figure 2*d***). They determined the 3D coordinates of particle centroids based on the 3D intensity distribution of their reconstructed image. To measure velocity, they fitted a Gaussian intensity distribution around each centroid and performed 3D correlations using only the centroid location (concise cross-correlation). Using this approach, they measured velocity distributions within a vortex ring and behind a boundary-layer tab.

Another procedure is to record multiple holograms from different axial directions. Barnhart et al. (1994) were the first to successfully implement HPIV to obtain a full volumetric 3D velocity field. Using near-forward scattering, off-axis holography (**Figure 2*a***), they used a single beam to illuminate their sample volume, airflow in a pipe, but collected scattered light from two near-forward directions to take advantage of the higher intensity. They used different reference beams for the first and second exposures to resolve directional ambiguity problems, but recorded the two holograms on the same emulsion. During analysis, their 3D velocity was determined using stereo-PIV procedures. Several groups followed with different variations of the multiviewing directions. Meng & Hussain (1995) introduced the in-line recording of a single hologram combined with multiple, off-axis viewing of the reconstructed images to determine the 3D coordinates of particles.

Two orthogonal off-axis holograms (**Figure 2*b***) were used in our laboratory (Tao et al. 2000, 2002; Zhang et al. 1997) to measure the 3D velocity distribution within a square duct. Their hybrid approach involved forward illumination to maximize the intensity of light scattered from particles and a slightly inclined, single reference beam for each view. To filter the illuminating

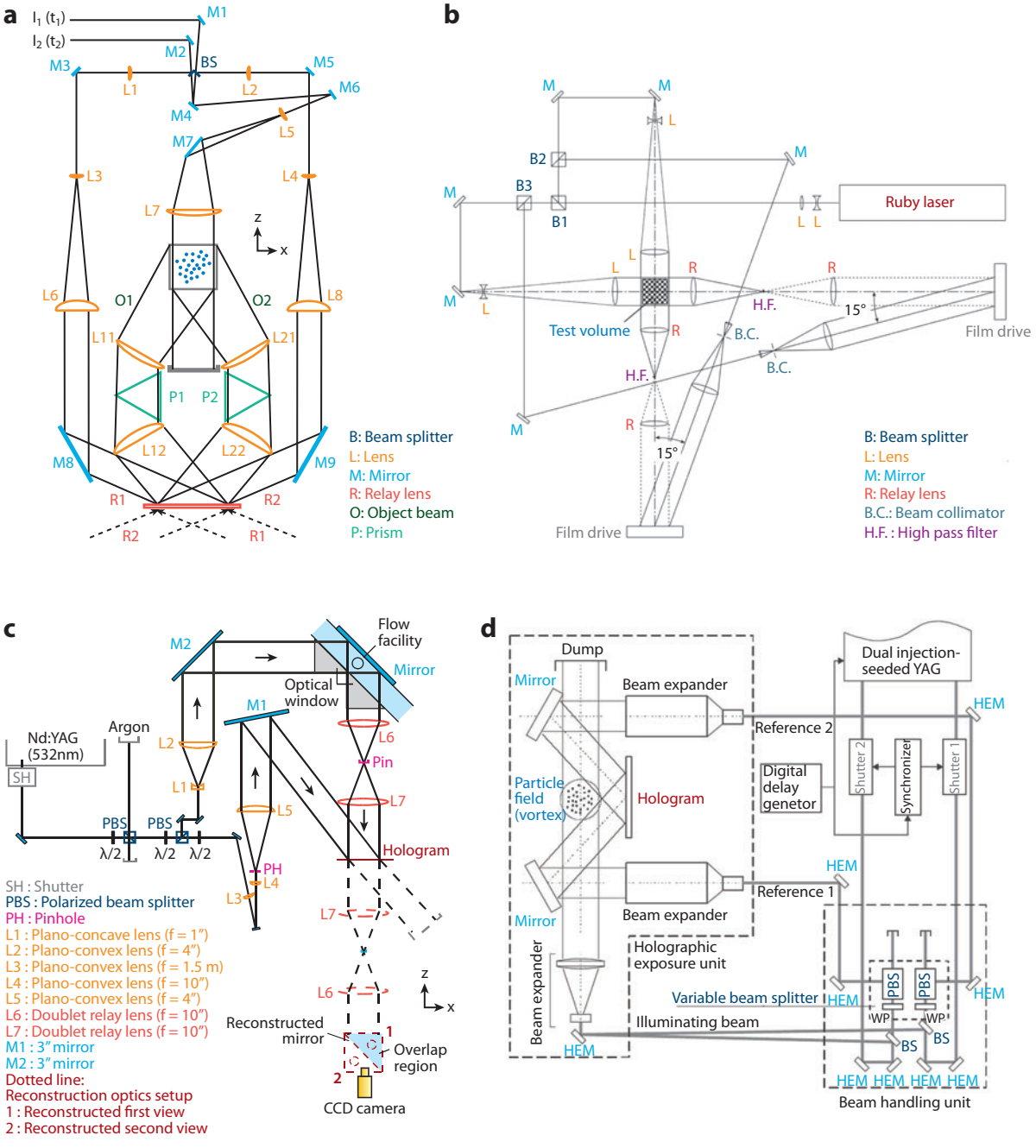

Figure 2

(*a*) Qualitative sketch of the phase-conjugate holographic particle-image velocimetry (HPIV) system of Barnhart et al. (1994). The directions of reconstruction waves are shown as dashed lines. (*b*) The hybrid off-axis HPIV system with dual orthogonal views of Zhang et al. (1997). Dotted arrows illustrate the direction of the reconstruction wave. (*c*) A schematic of the single-beam dual-view HPIV system of Sheng et al. (2003). Two orthogonal views are obtained by inserting a mirror on the wall of the sample volume. Dotted lines illustrate the optical setup during reconstruction. (*d*) The off-axis HPIV setup with 90° scattering from particles of Pu & Meng (2000). The same optics with the hologram rotated by 180° are used for reconstruction.

beam, and prevent it from overwhelming the scattered light, they inserted a high pass filter in the path of this beam, consisting of a pair of relay lenses, and a small mask in the focus of the first lens. This approach filtered out the illuminating beam but enabled most of the light scattered from particles to propagate undisturbed. Their reconstructed volume was scanned by a digital camera, and autocorrelation analysis was performed to determine the in-plane velocity components. The 3D velocity was obtained by combining the views, using the redundant component as a basis for precision matching. The database was used in several studies, as discussed below.

In an attempt to simplify the optical setup, Sheng et al. (2003) introduced the single-beam, two-views (**Figure 2*c***) approach, which maintained the advantages of recording two orthogonal views, but required only one window and one recording system. This method was based on placing a mirror in the test section that reflected the object beam at an angle of 45°. Particles located in the volume in which the incident and reflected beams overlapped were illuminated twice in perpendicular directions. Both views were recorded on the same off-axis hologram. The two views reduced the uncertainty in 3D coordinates of particles to within a few micrometers. Matching the two views, which required the precise determination of the mirror location and orientation, was the primary challenge in implementing this procedure. Malkiel et al. (2003) subsequently implemented this same approach while using digital in-line holography to study the swimming behavior of a marine copepod.

Several other creative methods should also be mentioned. Barnhart et al. (2002a,b, 2004a) introduced a quite different object conjugate reconstruction process. They used off-axis holography with near-forward scattering to record the holograms. However, instead of illuminating the hologram with a reference beam, they traversed a point source generated by the illumination through an optical fiber, in the vicinity of the hologram. Once this point source moved in the immediate vicinity of a particle in the original flow field, it mimicked the light scattered from this particle, and consequently reconstructed the original reference beam. The location of peak intensity, as measured by a detector, could then be used to position particles and measure their displacement in sparsely seeded flow fields.

Herrmann & Hinsch (2004) introduced a method referred to as light in flight holography to reduce the axial extent of a particle signature and reduce its impact on the reconstruction of particles located in other planes. Using an off-axis setup and an intentionally low coherence laser, they took advantage of spatial variations in the travel distance of the inclined reference beam to different sections of the hologram. An interference pattern could be obtained only when the path length of light scattered by particles did not differ from that of the reference beam by more than the coherence length of the laser (millimeter range). Consequently, light diffracted from particles located a certain distance from the hologram plane interfered only with the part of the reference beam that matched its path length. Illuminating small sections of the hologram then reconstructed particles located within the volumetric shell that matched the path length of the reference beam illuminating that section. Additional information on the procedures mentioned in this section can be found in several review articles (Arroyo & Hinsch 2008, Hinsch 2002, Royer 1997).

2. TRANSITION TO DIGITAL HOLOGRAPHY

Although the resolution of emulsions is at least an order of magnitude higher than that of digital recording media, the processes involved are cumbersome. Furthermore, the use of plates or film greatly limits the ability to study dynamic phenomena. Low-resolution cinematographic holography was introduced decades ago (Heflinger et al. 1978, Knox & Brooks 1969). However, recent advances in digital imaging have led to renewed interest in digital holography as a means of detecting and tracking particles and measuring 3D flows (Kebbel et al. 1999, Malkiel et al. 2003,

Meng et al. 2004, Owen & Zozulya 2000, Xu et al. 2001). Moreover, applications of digital holography have extended recently into microscopy. Owing to the limited resolution of digital media (3–15 μm, depending on the pixel size), almost all recent applications have involved in-line holography in two basic setups, depending on the properties of the sample volume. If one can maintain the wave front of the illuminating beam with minimal disturbance, a simple in-line hologram, in which the illuminating beam serves also as a reference beam, is sufficient and easy to implement. If the wave front of the illuminating beam is distorted to a level that it can no longer be used as a reference beam, another reference beam that does not pass through the distorting medium is required.

2.1. Mathematical Analysis of Acquisition and Reconstruction of Holograms

Mathematical models for the recording and reconstruction of in-line digital holograms based on the Fresnel approximation were introduced by Onural & Scott (1987) and expanded by Juptner and colleagues (Schnars & Juptner 2002, Schnars et al. 1999). Milgram & Li (2002) developed analysis tools for numerically reconstructing scanned film holograms. However, regardless of recording schemes, the intensity of light on the plane of an amplitude hologram, I_h, is a record interference between the complex reference wave $\tilde{R}$ and object wave $\tilde{O}(x_h, y_h)$:

$$I_h(x_h, y_h) = (\tilde{R} + \tilde{O})(\tilde{R}^* + \tilde{O}^*) = RR^* + \tilde{R}\tilde{O}^* + \tilde{R}^*\tilde{O} + \tilde{O}\tilde{O}^*, \quad (1)$$

where the asterisk indicates a complex conjugate and (x_h, y_h) represent points on the hologram ($z_h = 0$). The first term represents mean irradiance by the reference beam, $\tilde{R}\tilde{O}^*$ and $\tilde{R}^*\tilde{O}$ generate the interference patterns, and $\tilde{O}\tilde{O}^*$, often called the halo, contributes to noise. The resulting transmittance of the hologram after film development or the intensity distribution of the digital hologram can be expressed as $h(x, y) = h_0 + \alpha I_h(x_h, y_h)$, where h_0 is the inherent transmittance and α the exposure coefficient. For digital holography, $h_0 \approx 0$ and $\alpha \sim 1$. For film, $\alpha < 0$, and h_0 depends on film properties.

During reconstruction, a conjugate reference wave illuminates the hologram and is modulated by it, generating

$$\tilde{U}_r = \tilde{R}^* I_h = \underbrace{\|R\|^2 R^*}_{\substack{\text{Reference}\\ \text{Wave}}} + \underbrace{\|R\|^2 \tilde{O}^*}_{\substack{\text{Reconstructed}\\ \text{Object Wave}}} + \underbrace{\tilde{R}^{*2}\tilde{O}}_{\substack{\text{Virtual}\\ \text{Image}}} + R^*\tilde{O}\tilde{O}^*, \quad (2)$$

where the first term is a conjugate of the original wave, the second is a real image, the third represents the virtual image, and the last is the reference modulated by the halo. The real image, $\|R\|^2\tilde{O}^*$, propagates backward; i.e., the diverging wave of a point-source object becomes a converging wave that focuses at the same location. In general, the reference wave can be expressed as $\tilde{R} = |R|e^{j\phi_R(\vec{k},\vec{r})}$, where the phase, $\phi_R(\vec{k},\vec{r})$, has a known distribution, which depends only on location, $\vec{r}$, and $\vec{k} = (2n\pi/\lambda)\vec{e}_k$, the wave propagation vector, where n is the refractive index of the medium. The object wave, $\tilde{O} = |\tilde{O}(\beta, \tilde{U}_i, S)|e^{j\varphi(\beta,S)}e^{j\phi_o(\vec{k},\vec{r})}$, depends on $\vec{k}$ and $\vec{r}$ of the wave propagating from the object, the incident light illuminating the object, $\tilde{U}_i$, the scattering angle from the object, β, and the object optical characteristics, S. The first phase term represents scattering characteristics from the object, and $\phi_O(\vec{k},\vec{r})$ represents propagation to the recording medium. In the case of a small particle located at $\vec{r}_p$, $\tilde{O} \approx \|O(x_p, y_p)\|/\|\vec{r} - \vec{r}_p\|e^{j\vec{k}\cdot(\vec{r}-\vec{r}_p)}$. **Table 1** summarizes three characteristic conjugate reconstruction waves.

Table 1 Typical configurations of conjugate reconstruction waves used in digital holography

Configuration	Conjugate reconstruction wave at the hologram plane $z = 0$
In-line holography with a plane reference wave	$\tilde{R}^*(x_b, y_b) = A$, where A is the amplitude
In-line holography with a point-source reference (Xu et al. 2001)	$\tilde{R}^*(x_b, y_b) = Ae^{-j\vec{k}\cdot(\vec{r}_b - \vec{r}_0)}/\|\vec{r}_R - \vec{r}_0\|$, where r_0 and r_R are the location of point source and a point on the hologram, respectively
Off-axis holography with a plane reference wave	$\tilde{R}^*(x_b, y_b) = Ae^{-j(k_x \cos\theta + k_y \sin\theta)}$, where θ is the incident angle of reference wave

2.2. Digital Reconstruction Methods

When reconstruction is performed digitally, the optical field is approximated as diffraction from a 2D complex aperture, the hologram, which generates the optical field

$$\tilde{U}_r(x, y, z) = \iint_{x_b, y_b} \tilde{U}_r(\xi, \eta, z = 0)\left[-\frac{\partial G}{\partial n}(x - \xi, y - \eta, z)\right] d\xi d\eta. \quad (3)$$

Here, $\frac{\partial G}{\partial n}$ is the normal derivative of Green's function of wave equation propagation in a homogeneous medium, as evaluated at the aperture plane, $z = 0$. This kernel essentially represents the diffraction of a point source, and wave propagation through the hologram is expressed in the form of a 2D convolution integral of the kernel with the optical field of the hologram. The image in a certain depth is the irradiance field, i.e., $\tilde{U}_r\tilde{U}_r^*(x, y, z)$. Two kernel functions are frequently used, namely the Rayleigh-Sommerfeld formula,

$$-\frac{\partial G}{\partial n}(x, y; z) = \frac{1}{\lambda}\frac{\exp(-jk\sqrt{x^2 + y^2 + z^2})}{\sqrt{x^2 + y^2 + z^2}}\cos\theta, \quad (4)$$

where $\cos\theta = z/\sqrt{x^2 + y^2 + z^2}$, and is often assumed to be ~1 for simplicity, and the Kirchhoff-Fresnel approximation,

$$-\frac{\partial G}{\partial n}(x, y; z) = \frac{\exp(jkz)}{j\lambda z}\exp\left\{j\frac{k}{2z}[(x^2 + y^2)]\right\}. \quad (5)$$

The Kirchhoff-Fresnel expression can be obtained from the Rayleigh-Sommerfeld formula using binomial expansion and a paraxial approximation, i.e., $\sqrt{x^2 + y^2} \ll z$.

The convolution (Equation 3) can be performed either as an integral in the spatial domain, which is a cumbersome process, or as a multiplication in the frequency domain,

$$\tilde{U}_r(x, y, z) = \Im^{-1}[\Im(\tilde{U}_r) \cdot \tilde{G}], \quad (6)$$

where $\Im$ represents a Fourier transform and $\tilde{G} = \Im(\frac{\partial G}{\partial n})$.

When the flow field has a uniform background and contains only small particles, one has a more computationally efficient option, namely the use of a discretized analytic expression of the spectral representations of kernels. For the Rayleigh-Sommerfeld kernel, this expression is $G(f_x, f_y) = \exp(-j\frac{2\pi z}{\lambda}\sqrt{1 - \lambda^2 f_x^2 - \lambda^2 f_y^2})$, where $f_{x,y} = 1/x, y$, and its discrete form is $G(m, n) = \exp(-j\frac{2\pi z}{\lambda}\sqrt{1 - (\frac{\lambda m}{M\Delta x})^2 - (\frac{\lambda n}{N\Delta y})^2})$, where M and N are the total number of discretization points along the x and y axis, respectively. For the Kirchhoff-Fresnel kernel, the analytic expression is $G(f_x, f_y) = j\lambda\exp[-j\pi\lambda z(f_x^2 + f_y^2)]$, and its discretized form is $G(m, n) = j\lambda\exp\{-j\lambda z\pi[(\frac{m}{M\Delta x})^2 + (\frac{n}{N\Delta x})^2]\}$.

For both kernels, reconstruction is performed plane by plane with z, the axial distance from the hologram, as a parameter. **Figure 3*a*** shows a sample synthetic in-line hologram involving a collimated reference beam and an aperture with size D, which is located at z and generates uniform forward illumination. In the fringes, the high-frequency fluctuation is a function of $r^2/\lambda z$

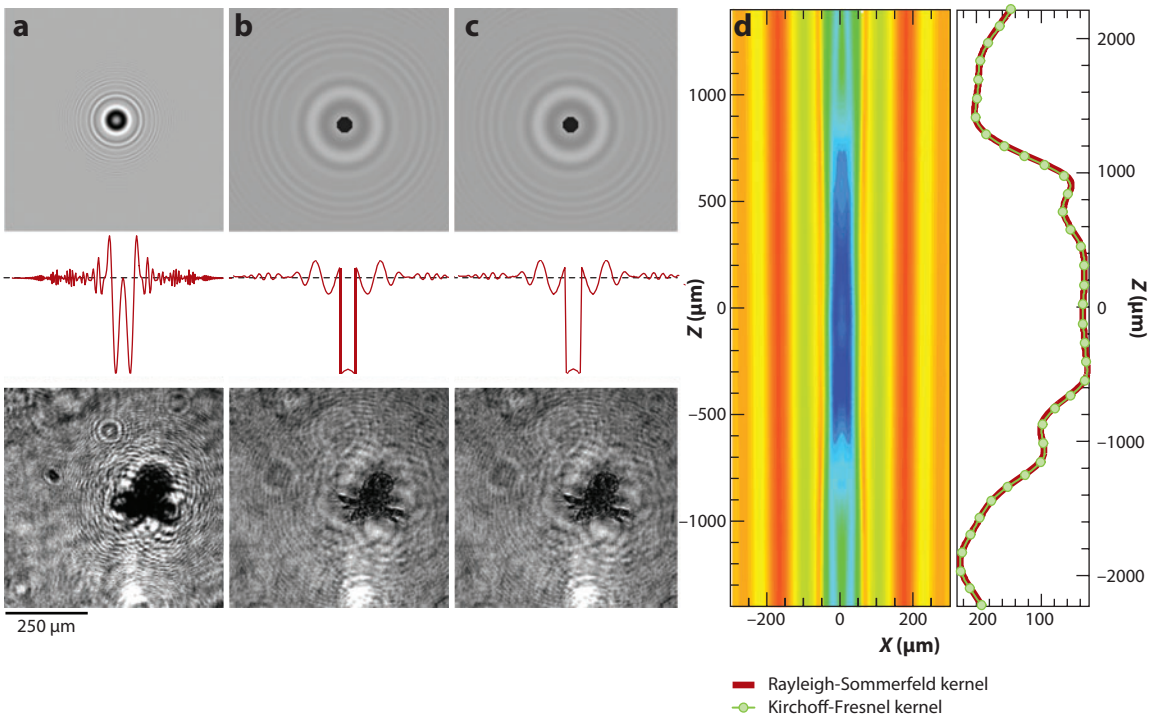

Figure 3

(*a*) Synthetic hologram (*top*) of a 2D disk aperture with an 81-μm (11-pixel) diameter located 20 mm from the hologram plane. (*Middle*) Intensity profile across the center of the synthetic hologram. (*Bottom*) A sample digital hologram of a free swimming nauplius recorded with a 10× magnification. (*b*) Digital reconstruction using the Kirchoff-Fresnel kernel. (*Top*) In focus reconstruction of the synthetic aperture in panel *a*. (*Middle*) Center cut of the irradiance profile. (*Bottom*) In focus reconstructed nauplius at $z = 3.345$ mm. (*c*) Digital reconstruction using the Rayleigh-Sommerfeld kernel. (*Top*) Reconstruction of the synthetic aperture shown in panel *a*. (*Middle*) Corresponding irradiance profile. (*Bottom*) Reconstructed image of the nauplius. (*d*) *x*-*z* distribution and centerline profile of the reconstructed irradiance field of the 2D synthetic aperture showing the depth-of-focus effect. The red line represents the Rayleigh-Sommerfeld kernel, and the green line represents the Kirchoff-Fresnel kernel.

(i.e., it encodes the depth of the object), whereas the low-frequency envelope is a function of $rD/\lambda z$ (i.e., it contains information on the size of the object). In focus reconstructions, using both kernels along with centerline cuts through their centers (**Figure 3*b*,*c***), confirming that as long as the paraxial approximation is valid, there is little difference between kernels. Because the real and virtual images are located symmetrically on both sides of the hologram, the virtual image generates a series of faint interference fringes in the real image plane and vice versa. These fringes have an adverse effect on the quality of images and may introduce a bias in some applications of holography to 3D velocity measurements (Ooms et al. 2008). **Figure 3*d*** is an axial cut through the center of the reconstructed image, showing the ∼1-mm long, elongated peak causing the DOF problem.

2.3. Digital Holographic Microscopy

Early attempts to implement digital holographic microscopy (DHM) were based on a lensless system, which imposed a stringent requirement for sensor pixel size. Xu et al. (2001) circumvented this problem by recording magnified interference fringes using a point-source reference wave and

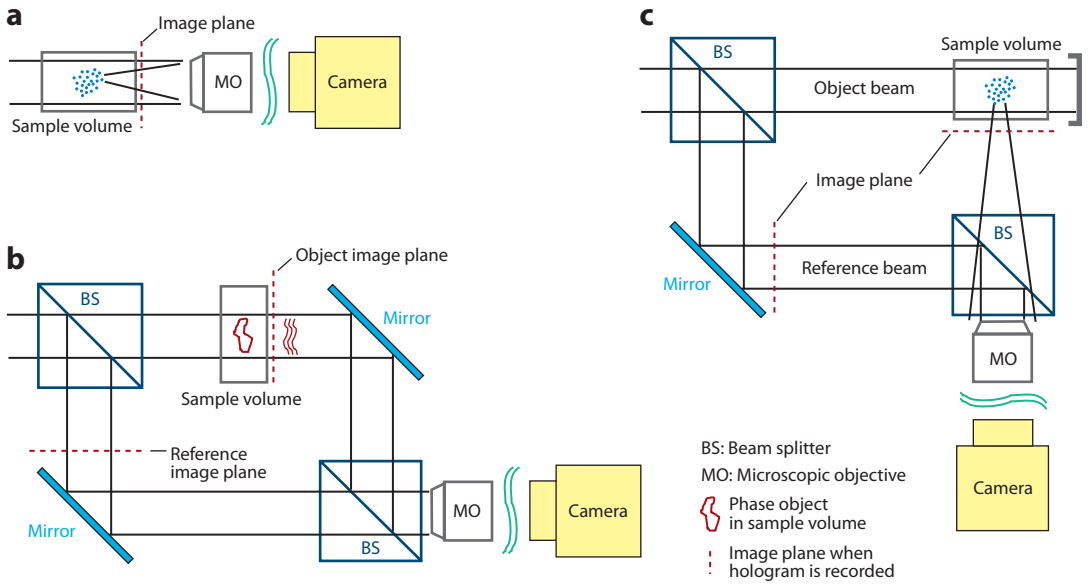

Figure 4

(*a*) Setup of in-line digital holographic microscopy (DHM), with the red dotted line indicating the image plane of the objective. (*b*) Optical layout of DHM based on Mach-Zehnder interferometry. The red line in the sample volume represents a phase object, e.g., a cell. (*c*) Optical layout of the hybrid digital holography with 90° side scattering from particles (Cao et al. 2008). The red dashed line indicates the image plane.

demonstrated that they could resolve micrometer-scale, 3D structures within a single cell or its 3D motion (Garcia-Sucerquia et al. 2006; Xu et al. 2001, 2002). The main advantage of this approach is its simple optical setup. However, data analysis is complicated for two reasons. First, the magnification of such a hologram is $M = z_R/z_o$, where z_R and z_o are the axial distances from the source of the reference and object beams, respectively, to the hologram. This magnification varies with the object depth, complicating the process of measuring 3D velocity and trajectories. Second, the numerical reconstruction algorithm is cumbersome.

Sheng et al. (2006) recorded magnified digital holograms using a transmission microscope setup, with the objective focusing on a plane located close to but outside of the sample volume (see **Figure 4*a***). This in-line setup was simple to implement and straightforward to reconstruct numerically. The optical field, U_R, recorded by a pixel array located at z_i (and subsequently reconstructed) was a magnified optical field of the image plane, U_H, which is located at z_o, with a phase correction, i.e.,

$$U_R(x_i, y_i, z_i) = \frac{1}{M} U_H\left(-\frac{x_i}{M}, -\frac{y_i}{M}\right) \exp\left[j\frac{k}{2M^2|z_0 - z_{lens}|}(x_i^2 + y_i^2)\right] \exp\left[j\frac{k}{2\,|z_i - z_{lens}|}(x_o^2 + y_o^2)\right]. \quad (7)$$

Here, $M = |z_i - z_{lens}|/|z_0 - z_{lens}|$ is the magnification of the microscope objective. The phase correction approaches 1 when M is sufficiently large. Tests demonstrated that in-line DHM successfully recorded and reconstructed several thousands of particles located within a sample whose depth extended to almost 1000 times the depth of field of a conventional microscope. Yet, it maintained the lateral spatial resolution of the conventional microscope over the entire volume. DHM was capable of detecting micrometer and submicrometer particles, which is impossible for lensless in-line holography, especially in liquid. They also demonstrated that magnifying the

holograms reduced (but did not eliminate) the DOF problem by an order of magnitude. The measured axial length of particle traces decreased to 2–10 diameters, decreasing with increasing magnification. Consequently, it was possible to determine the 3D particle coordinates from the intensity distribution within its reconstructed image, enabling 3D tracking and velocity measurements from a single view (Sheng et al. 2007, 2008, 2009).

In parallel, a large community has implemented DHM in a Mach-Zehnder interferometer setup (**Figure 4*b***) to record holograms, mostly of individual cells, and to examine subcellular structures (e.g., Carl et al. 2004; Colomb et al. 2005; Coppola et al. 2004; Dubois et al. 2002, 2004). Because the reference beam does not pass through the sample volume, this setup is for recording phase holograms, i.e., the diffraction of light while passing through a transparent medium with a different refractive index. Provided this refractive index is known, this procedure could be used to measure the thickness of a cell (e.g., Mann et al. 2005, Marquet et al. 2005). Techniques to improve resolution have also been introduced, e.g., illumination of the same sample from multiple angles (Choi et al. 2007, Mico et al. 2008) and submicrometer tomography with 0.6–1-μm axial resolution involving reflection microscopic holography at 20 different wavelengths (Kuhn et al. 2009).

3. TRACKING AND MEASUREMENTS OF PARTICLE DISPLACEMENT FROM DIGITAL HOLOGRAMS

Two approaches have been adapted for measuring the displacement of particles from reconstructed digital holograms of seeded flows. The first involves tracking individual particles, which can also be used to position them in space. The second approach involves correlation-based analysis, i.e., HPIV. For both, because reconstruction is performed plane by plane, a typical first step in data analysis involves segmentation to define the traces of each particle. Again, DOF has been the primary challenge. The most straightforward solution is to record multiple views, requiring careful calibrations of camera positions (Gopalan et al. 2008, Lu et al. 2008, Malkiel et al. 2003, Soria & Atkinson 2008). Another solution is based on the axial profile of the imaginary part of the reconstructed field. Because the in-focus image is presumably real, the root-mean-square value of the imaginary part should be minimal at the plane of focus of a particle (Pan & Meng 2003). The third popular solution is based on calculating the point of minimum intensity along the axis of the reconstructed particle trace, namely the centroid of the elongated ellipsoid. This approach has proven to be quite effective for DHM data due to the much shorter DOF (Kim & Lee 2007, 2008; Satake et al. 2005; Sheng et al. 2006, 2007, 2008, 2009). Furthermore, if it is used for velocity measurements, consistency in the procedure of detecting the centroid in two exposures cancels this problem in the displacement, but not for the particle location.

For holograms that cover a larger volume at a lower magnification, Meng and colleagues (Cao et al. 2008, Salazar et al. 2008) reduce the DOF by using a hybrid setup, which still involves in-line holography, but records 90° side scattering from particles (**Figure 4*c***). Ooms et al. (2006) have introduced another approach, which inserts a ring-shaped circular aperture between a pair of identical lenses, which are separated by twice their focal length. With optimized design, this spectral filter reduces the DOF by nearly a factor of five. The main drawback of this approach is a reduction in the intensity of light scattered by the particle. Finally, in the case of nonspherical particles (e.g., swimming organisms with complex shapes), the relation between the axial intensity distribution and plane of focus is not straightforward, and the axial intensity distribution may not have a distinct minimum. In such cases, the approximate depth location can be determined by edge detection, namely by selecting the plane with maximum edge contrast (Gopalan et al. 2008, Malkiel et al. 2004, Pfitsch et al. 2005, Sheng et al. 2007).

Many different procedures have been used for tracking particles to determine their velocity and/or trajectories. Matching exposures in reconstructed digital fields containing sparsely seeded flow fields have been based on the nearest-neighbor distance (NND) (Kim & Lee 2007, 2008; Satake et al. 2007). More complicated procedures are needed to match long tracks of particles, either in densely seeded flow fields or while following 3D trajectories of multiple particles for extended periods. Sheng et al. (2008, 2009) used multiple criteria when measuring the 3D velocity distribution in the inner part of a boundary layer. They first used 2D PIV on streamwise-spanwise slabs of a flow-field section to obtain characteristic planar velocity projections. Results and the location of a particle in the first exposure were used to define a spherical volume surrounding the most likely location of the second exposure. Then they used several criteria to determine which, among the particle traces located within the sphere, was the most likely second exposure. These criteria included deviations from PIV predictions; similarities in particle size, volume, and intensity distribution; and spatial smoothness in the velocity distribution based on the magnitude of 3D correlations between the first and second exposures, as well as constraints on the magnitude of wall-normal gradients of streamwise velocity that varied with elevation. Velocity measurements were based on the displacement of the intensity-weighted centroids of particles (results are discussed below).

With regard to tracking the long-time trajectories of marine dinoflagellates located in dense suspensions, Sheng et al. (2007) recorded high-speed, cinematic DHM data at a magnification of 20× to study their behavior. They used a series of Lagrangian criteria to track the helical trajectories of hundreds of cells for thousands of exposures. The guiding principle involved a trial-and-error process, which found the most likely trajectory over partial segments of 16 exposures among a maximum of six possible candidates for each time step, i.e., a maximum of 6^{16} trajectories, which were selected initially based on NND. Selection criteria included the smoothness of trajectory, the smoothness and upper bound of the 3D velocity and acceleration, and the similarity of cell size and shape. Gopalan et al. (2008) used different Lagrangian criteria to track crude-oil droplets and neutrally buoyant particles in a nearly isotropic turbulent flow. High-speed in-line digital holography, in part involving two perpendicular views, covered a volume of $50 \times 50 \times 50$ mm. In this case, the droplet concentration was sparse. A circularity filter aided in determining the droplets' location and size, as well as recognizing when droplet images overlapped. Matching criteria included 3D proximity, size, limits on acceleration, and the extrapolation of earlier trajectory segments. Automating the process enabled the tracking of more than 33,000 trajectories and the use of the statistical data to measure the turbulent diffusion of oil droplets.

Finally, we note that research to improve the accuracy of data-analysis procedures is still ongoing, including the development of procedures that follow substantially different paths. Ooms et al. (2008) attempted to deal with challenges involved with 3D correlation-based analysis in in-line digital holograms analyzed using the complex amplitude field (as opposed to intensity distributions). Included were potential problems of directional ambiguity and bias error introduced by the presence of a virtual image. Lobera & Coupland (2008) explored the application of optical diffraction tomography as a means to overcome the adverse effects of interference between multiscattering particles in a densely seeded flow. Lee et al. (2007) correlated an in-line microscopic hologram with the results of Lorentz-Mie scattering theory predictions to improve the accuracy in tracking and measuring the size of a single particle. The same approach was used to measure the size and refractive index of individual milk-fat globules in diluted samples and to track a particle through a gelled medium, also measuring its microrheological properties (Cheong et al. 2009a,b). Digital holography has also been used as a means of developing optical tweezers (e.g., Dufresne et al. 2001, Roichman et al. 2006, Roichman & Grier 2006).

4. SAMPLE RESULTS FROM RECENT APPLICATION IN FLUID MECHANICS AND PARTICLE DYNAMICS

4.1. Applications Related to Turbulence Research

Tao et al. (2000, 2002) used the optical setup shown in **Figure 2*b*** to obtain data to address a series of fundamental issues in the modeling of subgrid scale (SGS) stresses in large-eddy simulations. They performed the measurements in a 57×57 mm^2 square-duct channel flow and focused on the 3D velocity field away from the walls ($y > 5.25$ mm, $y^+ > 10^3$). Each of their instantaneous velocity distributions contained $136 \times 130 \times 128$ vectors with a spacing of 0.33 mm (with 66% overlap), 3.3 times the characteristic Kolmogorov scale ($\eta \approx 100$ μm). The velocity distributions were filtered by a 3D, spatial box filter with size of 33η, i.e., in the inertial range of turbulence, which provided the distributions of SGS stresses and SGS dissipation, along with the filtered vorticity and strain-rate tensor.

Statistical analysis confirmed that the most probable strain state was axisymmetric extension (i.e., pancake-like structures), and the most probable SGS stress state was axisymmetric contraction. The vorticity was aligned preferentially with the intermediate strain-rate tensor eigenvector, in agreement with previous publications, and was perpendicular to the most extensive SGS stress eigenvector. Joint probability density functions of relative angles were used to examine the alignments of the SGS stress eigenvectors relative to the vorticity and eigenvectors associated with eddy viscosity models, namely the filtered strain-rate tensor, and similarity/nonlinear models. The analysis led to a series of interesting trends. For example, unlike presumed relations, the SGS stress and strain-rate tensors were misaligned. The most extensive SGS stress eigenvector was preferentially aligned at 32° to the most contracting strain-rate eigenvector. The relative alignment of the other two stress- and strain-rate eigenvectors had a bimodal behavior, which depended on the vorticity magnitude and strain-rate topology. These observations were later confirmed using analysis of direct numerical simulation (DNS) data.

Using the same data, Van der Bos et al. (2002) examined the effects of SGS motions on invariants of the filtered deformation tensor $\tilde{A}_{ij} = \partial \tilde{u}_i / \partial x_j$ (where the $\sim$ indicates spatial filtering), namely $\tilde{Q} = -\tilde{A}_{im}\tilde{A}_{mi}/3$ and $\tilde{R} = -\tilde{A}_{im}\tilde{A}_{mk}\tilde{A}_{ki}/3$. Using conditional averaging, they quantified the significant effects of the SGS stress tensor on $\tilde{Q}$ and $\tilde{R}$, and compared them to effects of typical SGS stress models, showing both successes and failures, depending on the specific location in the ($\tilde{Q}$, $\tilde{R}$) plane, i.e., the characteristic local flow structure.

Recent experiments, which were performed in the same facility, utilized in-line DHM (**Figure 4*a***) with 10× magnification to examine the flow in the inner part of the boundary layer (Sheng et al. 2008, 2009). With DOF of three to five times the particle diameter (Sheng et al. 2006), the 3D velocity was obtained using single-view particle tracking. The number of resolved vectors in individual realizations varied from 2000 to 10,000 with a mean NND of $3 \sim 8$ wall units [$\delta_\vartheta = \nu/u_\tau = 17$ μm, $u_\tau = (\tau_w/\rho)^{0.5}$]. However, because most of the particles concentrated near the wall (<1 mm), the NND in the buffer layer was $\sim\delta_\vartheta$ in the wall-normal direction and $\sim 3\,\delta_\vartheta$ in streamwise and spanwise directions. The total sample volume size was $88\,\delta_\vartheta \times 145\,\delta_\vartheta \times 88\,\delta_\vartheta$ in the x, y, and z (streamwise, wall-normal, and spanwise) directions, respectively. The high-resolution DHM data enabled direct calculations of the instantaneous wall-shear-stress components directly from the slope of local velocity profiles in the viscous sublayer. Dividing the viscous sublayer into subvolumes of $150 \times 75 \times 150$ μm, and applying linear regression over all measured velocities within each volume, provided the local instantaneous wall stress at a resolution of $\sim 9\,\delta_\vartheta$ and an uncertainty of 8%. Consequently, these procedures provided the first simultaneous measurements of stress and 3D buffer-layer structures. Trends and magnitudes of normalized mean velocity and Reynolds stress agreed well with the DNS results of Kim et al. (1987).

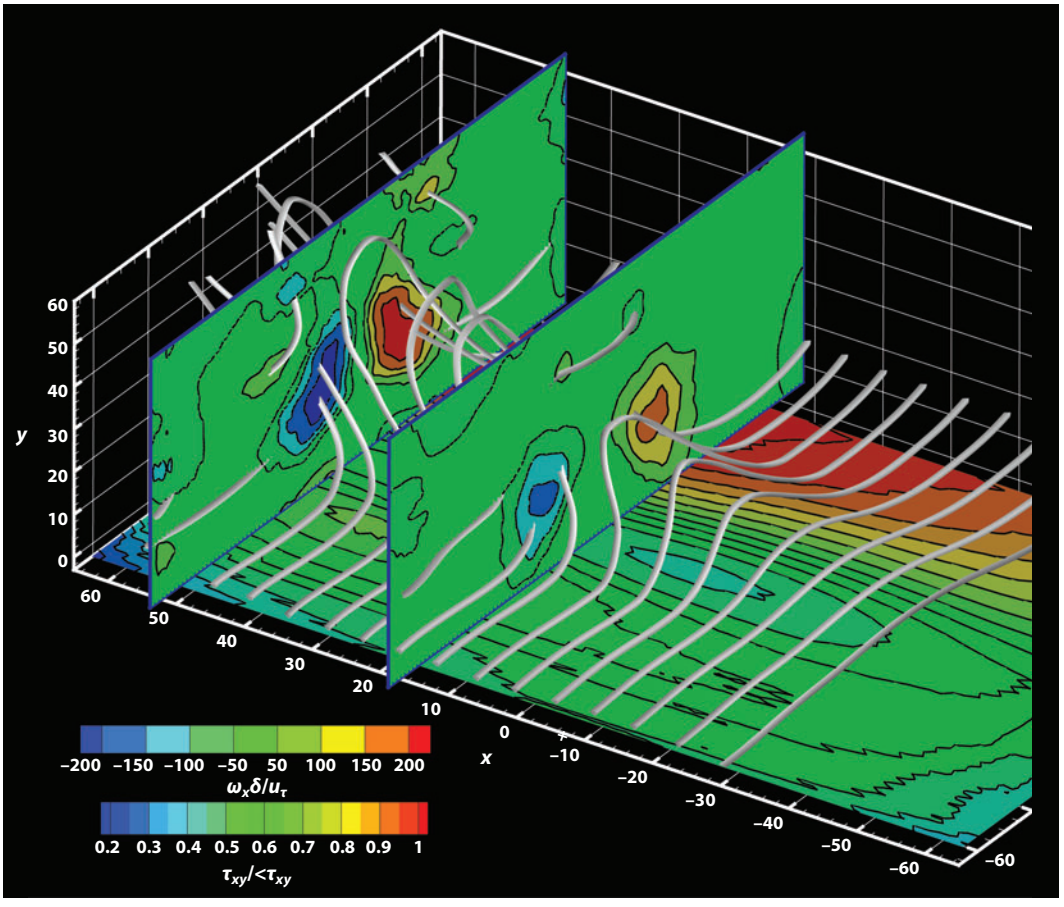

Figure 5

Conditionally averaged 3D flow structure and wall shear stress based on a local stress minimum, $\tau_{xy} < 0.6\langle\tau_{xy}\rangle$, at $x^+ = z^+ = 0$. (*Bottom contour plot*) Streamwise wall shear stress. To illustrate the 3D flow, several vortex lines (*gray*) are superimposed with distributions (*contours*) of $\omega_x\delta/u_\tau$ in two selected planes, $x^+ = 18$ and 50. Figure based on data presented in Sheng et al. 2009.

Rudimentary observations first classified the buffer-layer flow structures into three groups. Then, conditional sampling based on the existence of wall-shear-stress maxima or minima revealed that two types of 3D buffer-layer structures generated extreme stress events. The first structure (**Figure 5**) developed as spanwise vorticity lifted from the wall abruptly and within a short distance of approximately 10–20 δ_ϑ, creating initially a vertical arch. This arch was subsequently stretched vertically and in the streamwise direction, as the vortex lines illustrate, culminating in the formation of a pair of counter-rotating vortices with similar strength, which were inclined at an angle exceeding 45°. A wall-stress minimum existed under the point of initial lifting, and a pair of staggered maxima developed 35 δ_v downstream, on the downflow (outer) sides of the vortex pair. This structure existed not only in the conditionally averaged flow, but in 16.4% of the instantaneous realizations (40 cases out of 250) as well. Conditional velocity fluctuations and Reynolds stress distributions demonstrated the dominant mechanisms affecting momentum transport and the formation of wall-stress extremes. The formation of a vortex pair from lifted spanwise vorticity agreed with early experimental studies (e.g., Acarlar & Smith 1987a,b; Hinze 1975;

Kline et al. 1967; Robinson 1991; Willmarth & Tu 1967). The DHM data provided quantitative details and showed that the abrupt vertical lifting of spanwise vorticity was the primary contributor to the formation of the streamwise momentum deficit. The persistence of pairs of counter-rotating vortices with similar strength does not agree with the conclusions of several publications that have been based on DNS data (e.g., Jimenez & Pinelli 1999, Kim et al. 1987, Schoppa & Hussain 2002).

The second buffer-layer structure contributing to the generation of wall-stress maxima was a larger, single, slightly inclined (12°) streamwise vortex. It generated an elongated, strong stress maximum on one side, and a weak minimum on the other, and has been observed in 51 out of 250 of the realizations. The existence of slightly inclined, streamwise vortices in the buffer layer has been reported in several studies based on DNS (Adrian & Moin 1988, Jeong & Hussain 1995, Jimenez & Pinelli 1999, Kim et al. 1987, Kravchenko et al. 1993, Schoppa & Hussain 2002).

Svizher & Cohen (2006) implemented film-based off-axis holography to study the evolution of artificially generated hairpin vortices in a plane Poiseuille airflow. The HPIV data were utilized to obtain the instantaneous topology of the hairpin vortex along with velocity distributions. Results supported the view that the generation of hairpins was governed by the base-flow shear strain and the existence of a sufficiently large initial disturbance. Recently, Cao et al. (2008) and Salazar et al. (2008) used the setup shown in **Figure 4*c*** to measure the spatial distribution of particles in isotropic turbulence and compared the results with DNS predictions. The experiments were performed in a special isotropic turbulence facility containing air, and consisted of measuring the location of several hundred 6-μm hollow glass spheres in a 1-cm^3 volume. They quantified concentration fluctuations using the radial distribution function, namely the probability of finding a second particle in a given separation distance from a test particle. The results showed good agreement between the radial distribution function predictions of the DNS and the experimental data, despite interpretation challenges.

Gopalan et al. (2008) used high-speed digital holography cinematography to study the turbulent diffusion of slightly buoyant, 0.5–1.2-mm-diameter, diesel droplets and 50-μm-diameter neutral density particles in nearly isotropic turbulence (see the samples shown in **Figure 6**). The root-mean-square values of horizontal droplet velocity exceeded those of the fluid at all conditions, whereas the droplet vertical velocity fluctuations were higher than those of the fluid only at a high turbulence level. The turbulent diffusion coefficient was calculated by integrating the ensemble-averaged Lagrangian velocity autocovariance. They examined its trends as a function of the ratio of turbulence intensity to the droplet quiescent rise velocity (u'/Uq). Results showed that the diffusion coefficients in the horizontal and vertical directions were lower than those of the fluid at low normalized turbulence intensity, but they exceeded it with increasing turbulence level. For most of the conditions, the horizontal diffusion exceeded vertical levels.

4.2. Sample Laboratory Biological Applications

In this section we confine ourselves to dynamic phenomena, namely swimming behavior of aqueous organisms and related flow fields. Malkiel et al. (2003) measured the behavior and 3D flow around a swimming copepod, utilizing two perpendicular in-line digital holography views (**Figure 7*a***). A mirror attached to the wall, similar to that shown in **Figure 2*c*** (but using an in-line setup), enabled them to record both views on the same CCD (charge-coupled device) array. In addition to the copepod, the flow was seeded with 20-μm polystyrene spheres, and they measured the 3D velocity field surrounding the copepod. By combining reconstructed frames, shifted so that the image of the copepod was approximately fixed, the seed particles also visualized the flow in the

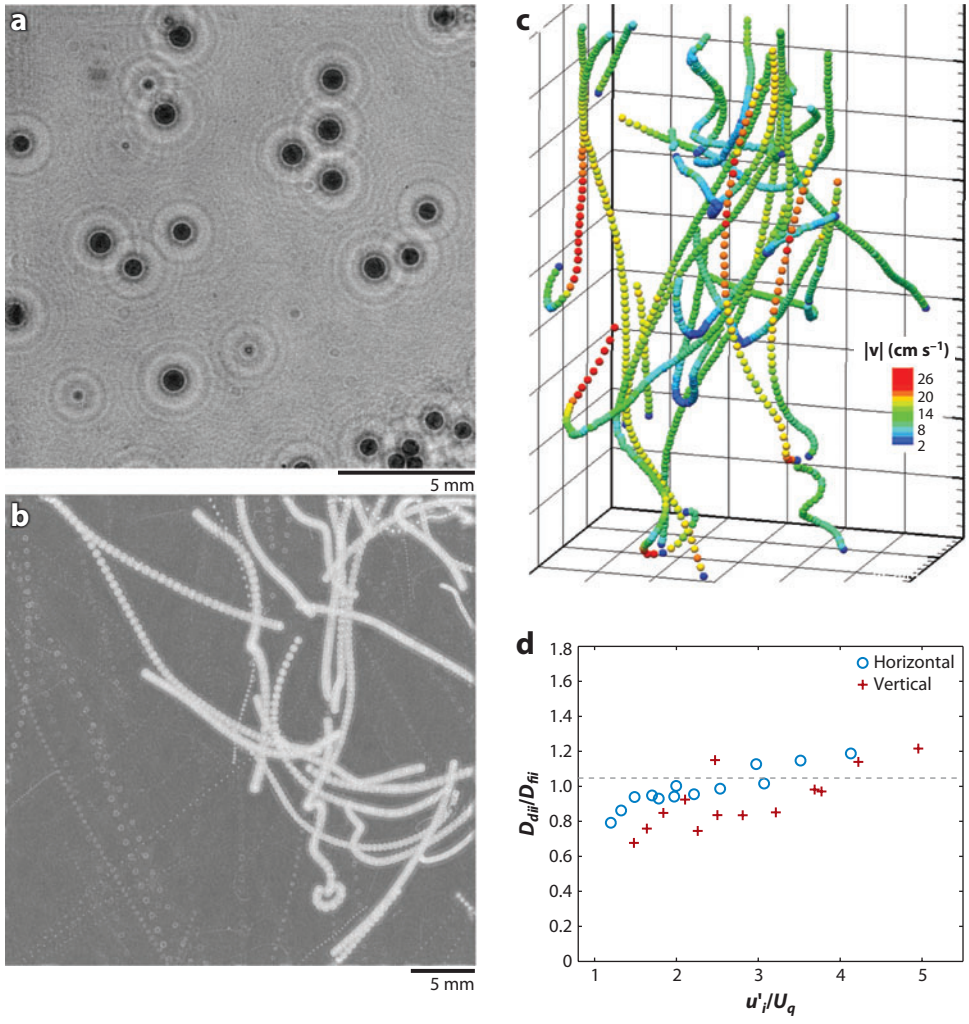

Figure 6

(*a*) Sample reconstructed image of in-focus oil droplets located in an isotropic turbulent flow field ($Re_\lambda = 214$). (*b*) Droplet trajectories recorded over 1s at 250 frames per second. Only one of every four droplets is shown for clarity. (*c*) 3D trajectories of the droplets shown in panel *b*, color-coded with the magnitude of instantaneous velocity. Grid: 4 mm. (*d*) Droplet horizontal and vertical diffusion coefficients normalized by the corresponding fluid diffusion coefficients as a function of the ratio of turbulence intensity to the droplet quiescent rise velocity, u_i'/U_q (Gopalan et al. 2008).

animal reference frame (**Figure 7*b***). Results demonstrated the formation of a recirculating flow pattern in the vicinity of the copepod, which was the result of the copepod sinking while generating a downward feeding current. The velocity distribution was used to estimate the excess weight of the copepod (weight minus buoyancy -7.2×10^{-9} N), and the propulsive force generated by its appendages (1.8×10^{-8} N). The holographic movies also showed that the copepod sank for several seconds and then executed a short hop upward and resumed sinking. Without such hops, the copepod would remain submerged within the same recirculating fluid, and its feeding current would not bring new food.

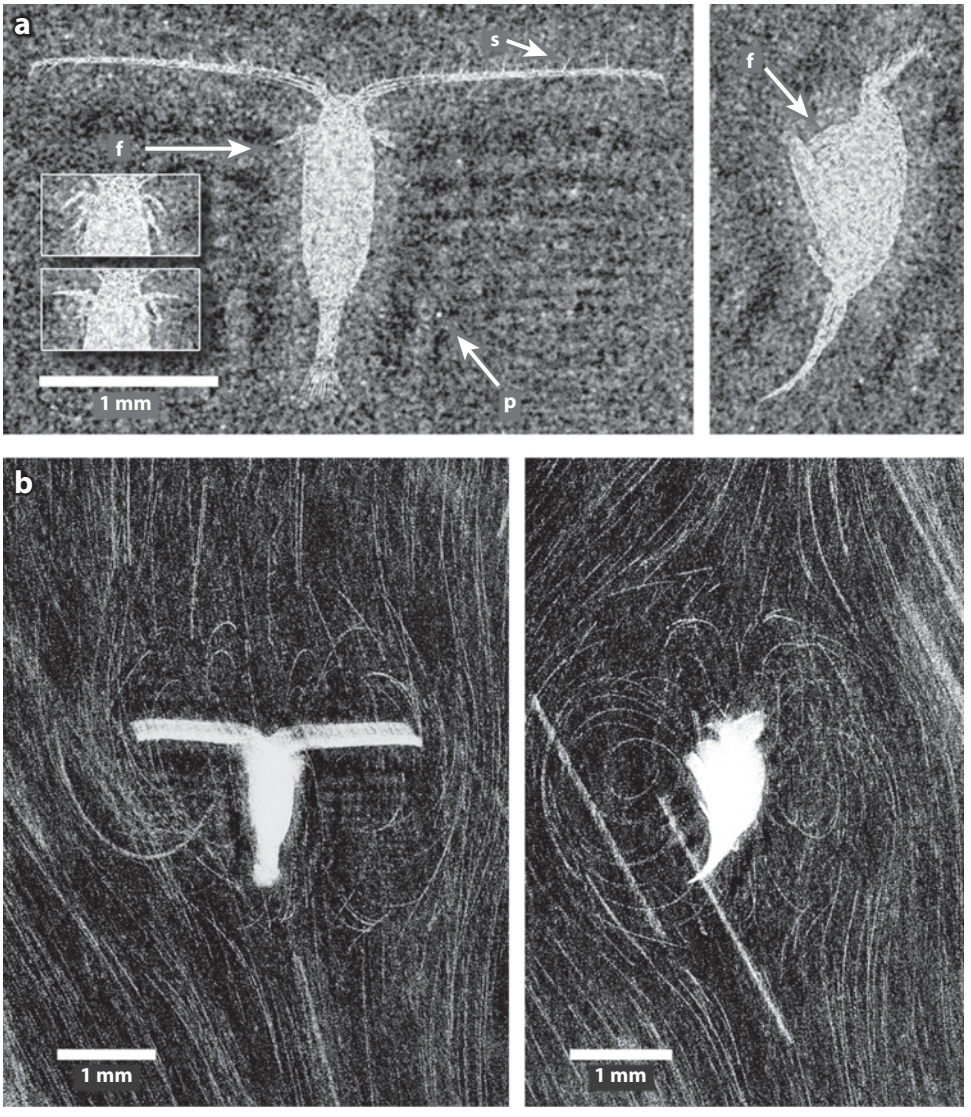

Figure 7

(*a*) In-focus, numerically reconstructed, dorsal (*left panel*) and lateral (*right panel*) views of the same swimming copepod. Highlighted with arrows are the setae (s) on antennule, feeding appendages (f), and a tracer particle (p) (there are many). The insets show the feeding appendages in upstroke and downstroke positions. (*b*) Particle streaks in the copepod reference frame obtained by combining 130 reconstructed images in the frame of the copepod. In all cases, the dorsal and lateral views are in focus (Malkiel et al. 2003).

Sheng et al. (2007) used cinematic DHM to characterize the swimming of thousands of marine dinoflagellates located within dense suspensions (see **Figure 8**). They focused on the mixotrophic dinoflagellate *Karlodinium veneficum*, the heterotrophic dinoflagellate *Pfiesteria piscicida*, and organisms on which they prey. NND analysis showed that predator and prey cells were randomly distributed relative to themselves, but predators clustered around their prey. Both dinoflagellate species exhibited a complex, quite different, and highly variable swimming behavior. When

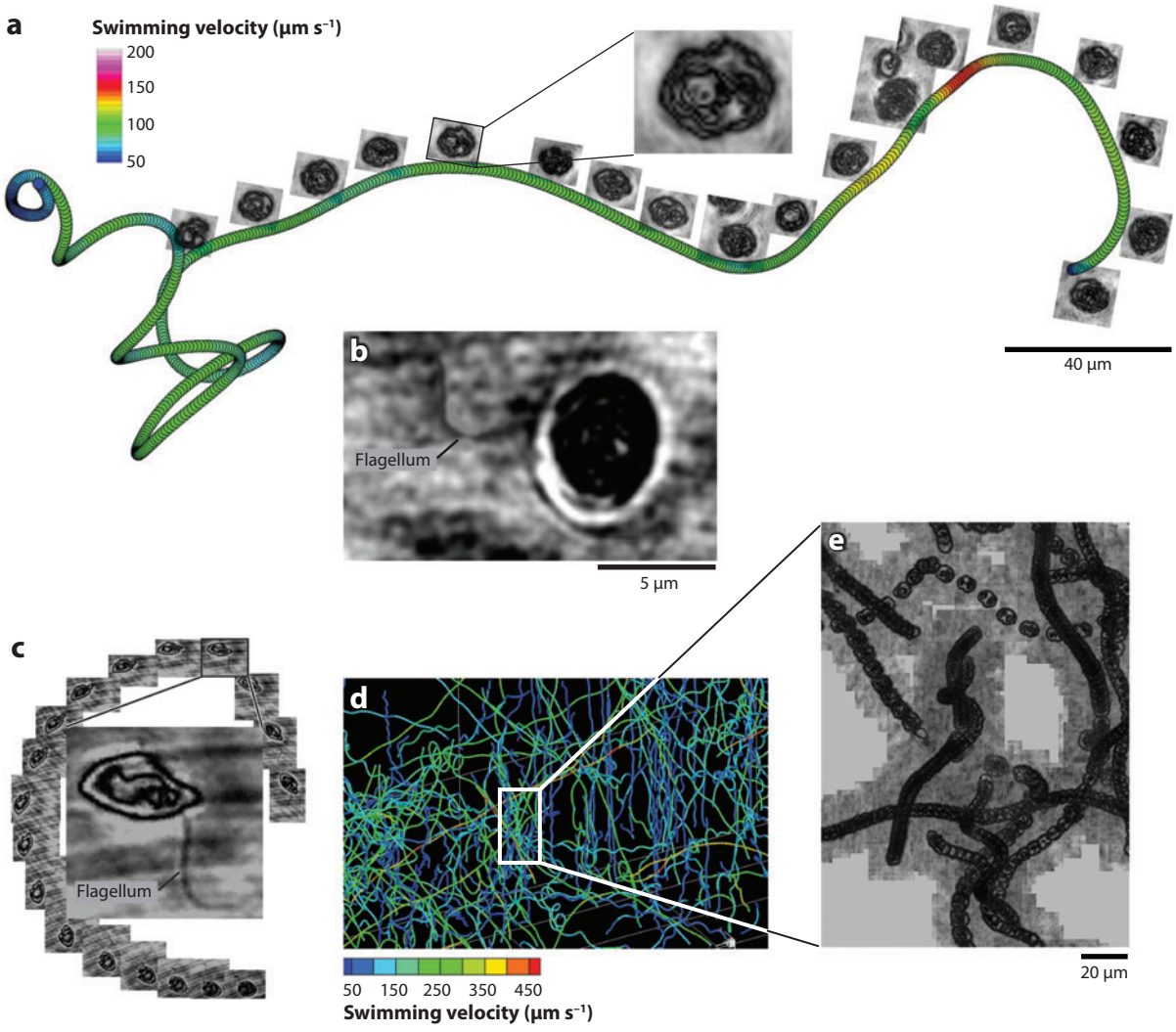

Figure 8

(*a*) A 3D trajectory of *Karlodinium veneficum*, color coded with swimming velocity, superimposed with in-focus images sampled every 40 time steps (0.33 s). (*Insets*) Reconstructed images of *K. veneficum* showing details of cell physiology (Sheng et al. 2007). (*b*) Sample reconstruction showing the ~200-nm longitudinal flagellum of *K. veneficum* (*marked by an arrow*). (*c*) Time series with 1/60-s interval of spiraling *Oxyrrhis marina*, clearly showing the 200-nm longitudinal flagellum. The center image shows an enlarged exposure. (*d*) Part of a 3-mm-deep sample volume showing trajectories of *K. veneficum* color coded with swimming velocity. (*e*) Close-up of part of the sample volume, which is marked by the white box in panel *d*. In-focus images obtained by an autofocusing process are superimposed to show details of cell-cell interactions.

presented with its prey, the slower *K. veneficum* reduced its velocity, radius, and pitch but increased its angular velocity. Conversely, the faster *P. piscicida* increased its speed, radius, and angular velocity. These different predation strategies are still a subject of ongoing research. Before concluding, we note that the images clearly show the location and shape of the longitudinal flagellum of these organisms (two samples are shown), despite the fact that this 200-nm flagellum falls well below the resolution limit of the microscope objective.

4.3. Field Applications

Fugal et al. (2004) mounted an in-line digital holography system under the wing of an aircraft to perform in situ measurements of atmospheric cloud particles. Relying on short exposure times, they recorded holograms in daylight. Preliminary data included reconstructed images of water

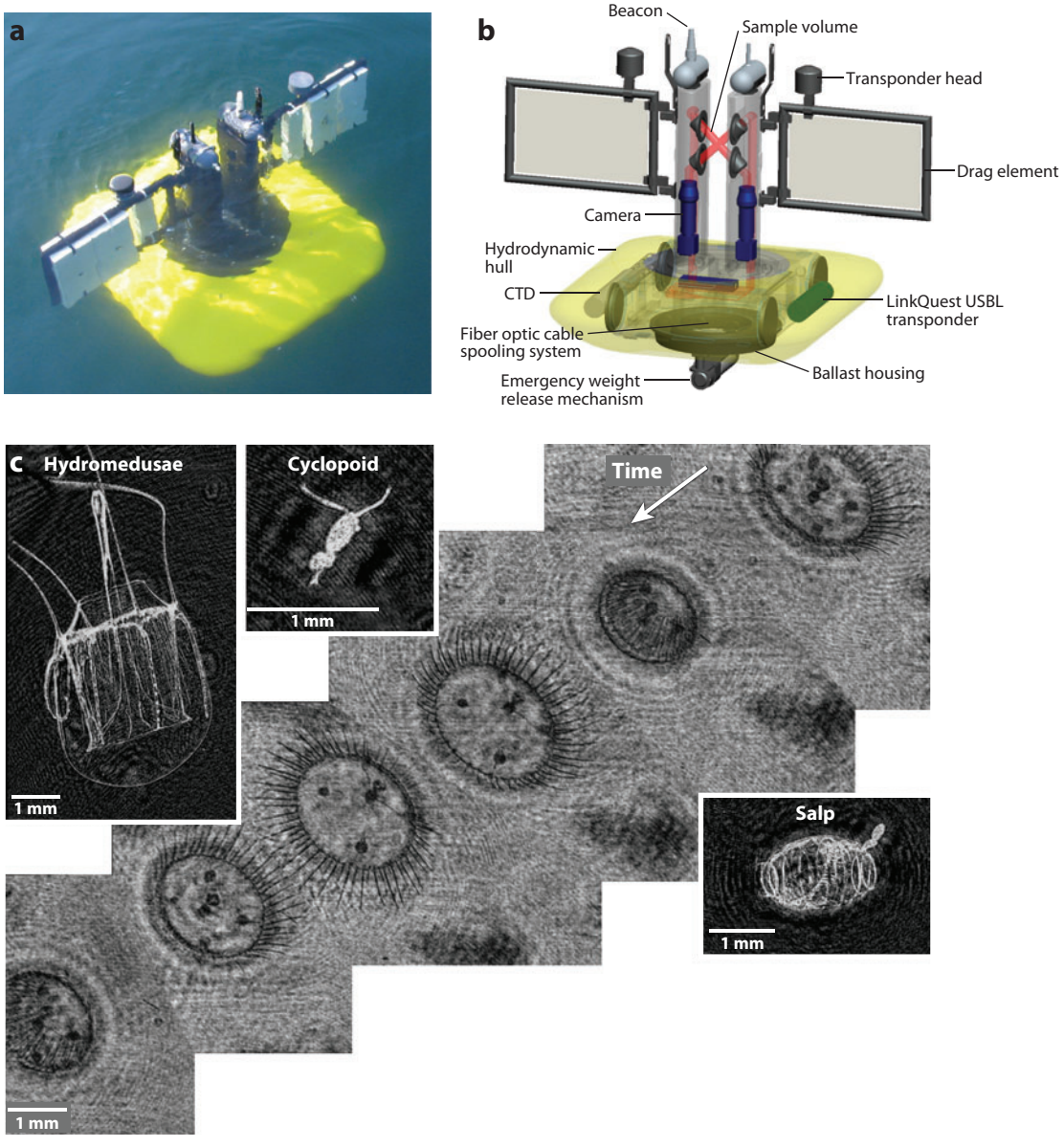

Figure 9

(*a*,*b*) A sketch and a picture of the free-drifting digital submersible holocamera. Fin height is 60 cm, and the gap between fins is 10 cm. (*c*) A sample 15-Hz time series of reconstructed images of a free-swimming small medusa captured during recent deployment. The motion of cilia is clearly captured. (*Insets*) Samples of other organisms.

droplets and ice crystals. Early oceanic deployments provided statistics on size distributions of particles at various depths (O'Hern et al. 1988). The next system (Katz et al. 1999, Malkiel et al. 1999) had a large battery and a 100-m film roll of 70-mm film, which enabled the acquisition of 300 holograms in each deployment. This system was deployed several times, either from the side of a boat or by being attached to the top of a manned submersible in the Gulf of Maine (Malkiel et al. 2004, 2006). To obtain meaningful statistics, it was essential to develop an automated system that scanned the reconstructed field, extracted in-focus images, measured their location, and classified them. These procedures were implemented to analyze more than 143 holograms, each resolving 5000–10,000 particles, including intermingling copepod species (e.g., calanoids, cyclopoids, and harpacticoids), nauplii, diatoms, and 10-μm to 5000-μm particles. NND statistics of the small particles showed a random distribution, but detritus particles clustered in several layers below the pycnocline. A submersible, film-based holography system, which utilized both in-line and off-axis holography, was developed by Watson et al. (2001) (see also Hobson & Watson 2002). The use of a high-power laser enabled them to extend the sample volume of the off-axis view, which had a resolution of ∼100 μm, potentially up to 10^5 cm^3. The in-line view was smaller, but had a higher resolution. The same group has recently assembled a compact submersible digital system (Sun et al. 2007, 2008) that can be deployed at depths exceeding 1 km.

Submersible digital holography enables the acquisition of in situ holographic movies. However, the sample volume is smaller, and resolution is lower, requiring a compromise either in volume size or resolution. A compact free-drifting digital holocamera is shown in **Figure 9**, along with sample images of marine organisms (Pfitsch et al. 2005, 2007). This system simultaneously records two in-line holograms of a volume located between the vertical fins. A single optical fiber, which is released from the platform, transmits multiplexed data to the research vessel from the cameras and other on-board sensors. The system location is monitored acoustically. The system can record perpendicular views at the same magnification, or parallel views at different magnifications. When deployed as a free drifter, two drag-generating elements minimize the relative motion. In currents of 20 cm s^{-1}, the relative velocity is ∼1 cm s^{-1}, enabling observations on behavior.

In conclusion, the recent surge in applications of digital holography is a result of technological advancements catching up with long-term scientific needs to resolve 3D motions and structures in biology, fluid, and particle dynamics. We believe that the relatively simple optical setups, which facilitate integration with other instruments, will lead to further developments and adaptation as a research tool in many fields.

DISCLOSURE STATEMENT

Some of the research described in this paper has been performed under U.S. government grants awarded to the first author. Some of the material presented in this paper represents ongoing research performed by the authors.

ACKNOWLEDGMENT

We would like to express our gratitude to the National Science Foundation and The Office of Naval Research for their term support of the effort to develop holography as a research tool.

LITERATURE CITED

Acarlar MS, Smith CR. 1987a. A study of hairpin vortices in a laminar boundary layer. 1. Hairpin vortices generated by a hemisphere protuberance. *J. Fluid Mech.* 175:1–41

Acarlar MS, Smith CR. 1987b. A study of hairpin vortices in a laminar boundary layer. 2. Hairpin vortices generated by fluid injection. *J. Fluid Mech.* 175:43–83

Adrian RJ. 1991. Particle imaging techniques for experimental fluid mechanics. *Annu. Rev. Fluid Mech.* 23:261–304

Adrian RJ, Moin P. 1988. Stochastic estimation of organized turbulent structure: homogeneous shear flow. *J. Fluid Mech.* 190:531–59

Arroyo MP, Hinsch KD. 2008. Recent developments of PIV towards 3D measurements. In *Particle Image Velocimetry: New Developments and Recent Applications*, ed. A Schröder, CE Willert, pp. 127–54. New York: Springer

Barnhart DH, Adrian RJ, Papen GC. 1994. Phase-conjugate holographic system for high-resolution particle-image velocimetry. *Appl. Opt.* 33:7159–70

Barnhart DH, Chan VSS, Halliwell NA, Coupland JM. 2002a. Holographic velocimetry using object-conjugate reconstruction (OCR): a new approach for simultaneous, 3D displacement measurement in fluid and solid mechanics. *Exp. Fluids* 33:770–80

Barnhart DH, Halliwell NA, Coupland JM. 2002b. Object conjugate reconstruction (OCR): a step forward in holographic metrology. *Proc. R. Soc. Lond. Ser. A* 458:2083–97

Barnhart DH, Halliwell NA, Coupland JM. 2004a. Holographic velocimetry with object conjugate reconstruction (OCR): simultaneous velocity mapping in fluid and solid mechanics. *Proc. R. Soc. Lond. Ser. A* 460:2089–104

Barnhart DH, Koek WD, Juchem T, Hampp N, Coupland JM, Halliwell NA. 2004b. *Bacteriorhodopsin* as a high-resolution, high-capacity buffer for digital holographic measurements. *Meas. Sci. Technol.* 15:639–46

Cao L, Pan G, de Jong J, Woodward S, Meng H. 2008. Hybrid digital holographic imaging system for three-dimensional dense particle field measurement. *Appl. Opt.* 47:4501–8

Carder KL. 1979. Holographic micro-velocimeter for use in studying ocean particle dynamics. *Opt. Eng.* 18:524–25

Carder KL, Steward RG, Betzer PR. 1982. In situ holographic measurements of the sizes and settling rates of oceanic particulates. *J. Geophys. Res. Oceans Atmos.* 87:5681–85

Carl D, Kemper B, Wernicke G, von Bally G. 2004. Parameter-optimized digital holographic microscope for high-resolution living-cell analysis. *Appl. Opt.* 43:6536–44

Cheong FC, Duarte S, Lee SH, Grier DG. 2009a. Holographic microrheology of polysaccharides from *Streptococcus mutans* biofilms. *Rheol. Acta* 48:109–15

Cheong FC, Xiao K, Grier DG. 2009b. Technical note: characterizing individual milk fat globules with holographic video microscopy. *J. Dairy Sci.* 92:95–99

Choi W, Fang-Yen C, Badizadegan K, Oh S, Lue N, et al. 2007. Tomographic phase microscopy. *Nat. Methods* 4:717–19

Collier RJ, Burckhardy CB, Lin LH. 1971. *Optical Holography*. New York: Academic

Colomb T, Durr F, Cuche E, Marquet P, Limberger HG, et al. 2005. Polarization microscopy by use of digital holography: application to optical-fiber birefringence measurements. *Appl. Opt.* 44:4461–69

Coppola G, Ferraro P, Iodice M, De Nicola S, Finizio A, Grilli S. 2004. A digital holographic microscope for complete characterization of microelectromechanical systems. *Meas. Sci. Technol.* 15:529–39

Dubois F, Minetti C, Monnom O, Yourassowsky C, Legros JC, Kischel P. 2002. Pattern recognition with a digital holographic microscope working in partially coherent illumination. *Appl. Opt.* 41:4108–19

Dubois F, Requena MLN, Minetti C, Monnom O, Istasse E. 2004. Partial spatial coherence effects in digital holographic microscopy with a laser source. *Appl. Opt.* 43:1131–39

Dufresne ER, Spalding GC, Dearing MT, Sheets SA, Grier DG. 2001. Computer-generated holographic optical tweezer arrays. *Rev. Sci. Instrum.* 72:1810–16

Erf RK. 1974. *Holographic Nondestructive Testing*. New York: Academic

Fabry EP. 1998. 3D holographic PIV with a forward-scattering laser sheet and stereoscopic analysis. *Exp. Fluids* 24:39–46

Fugal JP, Shaw RA, Saw EW, Sergeyev AV. 2004. Airborne digital holographic system for cloud particle measurements. *Appl. Opt.* 43:5987–95

Gabor D. 1948. A new microscopic principle. *Nature* 161:777–78

Gabor D. 1949. Microscopy by reconstructed wave fronts. *Proc. R. Soc. Lond. Ser. A* 197:454–87
Garcia-Sucerquia J, Xu WB, Jericho SK, Klages P, Jericho MH, Kreuzer HJ. 2006. Digital in-line holographic microscopy. *Appl. Opt.* 45:836–50
Gopalan B, Malkiel E, Katz J. 2008. Experimental investigation of turbulent diffusion of slightly buoyant droplets in locally isotropic turbulence. *Phys. Fluids* 20:095102
Gunter P, Huignard JP. 1989. *Photorefractive Materials and Their Applications*. Berlin: Springer-Verlag
Heflinger LO, Stewart GL, Booth CR. 1978. Holographic motion pictures of microscopic plankton. *Appl. Opt.* 17:951–54
Herrmann SF, Hinsch KD. 2004. Light-in-flight holographic particle image velocimetry for wind-tunnel applications. *Meas. Sci. Technol.* 15:613–21
Hinsch KD. 2002. Holographic particle image velocimetry. *Meas. Sci. Technol.* 13:R61–72
Hinze JO. 1975. *Turbulence*. New York: McGraw-Hill. 790 pp.
Hobson PR, Watson J. 2002. The principles and practice of holographic recording of plankton. *J. Opt. A* 4:S34–49
Jeong J, Hussain F. 1995. On the identification of a vortex. *J. Fluid Mech.* 285:69–94
Jimenez J, Pinelli A. 1999. The autonomous cycle of near-wall turbulence. *J. Fluid Mech.* 389:335–59
Katz J. 1984. Cavitation phenomena within regions of flow separation. *J. Fluid Mech.* 140:397–436
Katz J, Donaghay P, Zhang J, King S, Russell K. 1999. Submersible holocamera for detection of particle characteristics and motions in the ocean. *Deep-Sea Res. I* 46:1455–81
Katz J, O'Hern TJ, Acosta A. 1984. An underwater holographic camera system for detection of microparticulates. *Proc. ASME Cavitation Polyphase Flow Forum*, ed. JW Hoyt, pp. 22–25, New York: ASME
Kebbel V, Adams M, Hartmann HJ, Juptner W. 1999. Digital holography as a versatile optical diagnostic method for microgravity experiments. *Meas. Sci. Technol.* 10:893–99
Kim J, Moin P, Moser R. 1987. Turbulence statistics in fully-developed channel flow at low Reynolds number. *J. Fluid Mech.* 177:133–66
Kim S, Lee SJ. 2007. Measurement of 3D laminar flow inside a micro tube using micro digital holographic particle tracking velocimetry. *J. Micromech. Microeng.* 17:2157–62
Kim S, Lee SJ. 2008. Effect of particle number density in in-line digital holographic particle velocimetry. *Exp. Fluids* 44:623–31
Kinoshita K. 1992. Novel use of thermoplastic plates for rewritable holographic stereograms. *Jpn. J. Appl. Phys.* 31:1677–81
Kline SJ, Reynolds WC, Schraub FA, Rundstadler PW. 1967. The structure of turbulent boundary layers. *J. Fluid Mech.* 30:741–77
Knox C. 1966. Holographic microscopy as a technique for recording dynamic microscopic subjects. *Science* 153:989–90
Knox C, Brooks RE. 1969. Holographic motion picture microscopy. *Proc. R. Soc. Lond. Ser. B* 174:115–21
Konrath R, Schroder W, Limberg W. 2002. Holographic particle image velocimetry applied to the flow within the cylinder of a four-valve internal combustion engine. *Exp. Fluids* 33:781–93
Kravchenko AG, Choi HC, Moin P. 1993. On the relation of near-wall streamwise vortices to wall skin friction in turbulent boundary layers. *Phys. Fluids A* 5:3307–9
Kuhn J, Montfort F, Colomb T, Rappaz B, Moratal C, et al. 2009. Submicrometer tomography of cells by multiple-wavelength digital holographic microscopy in reflection. *Opt. Lett.* 34:653–55
Lee SH, Roichman Y, Yi GR, Kim SH, Yang SM, et al. 2007. Characterizing and tracking single colloidal particles with video holographic microscopy. *Opt. Exp.* 15:18275–82
Lobera J, Andres N, Arroyo MP, Quintanilla M. 2004. Dual holographic interferometry for measuring the three velocity components in a fluid plane. *Appl. Opt.* 43:3535–42
Lobera J, Coupland JM. 2008. Optical diffraction tomography in fluid velocimetry: the use of a priori information. *Meas. Sci. Technol.* 19:074013
Lozano A, Kostas J, Soria J. 1999. Use of holography in particle image velocimetry measurements of a swirling flow. *Exp. Fluids* 27:251–61
Lu J, Fugal JP, Nordsiek H, Saw EW, Shaw RA, Yang W. 2008. Lagrangian particle tracking in three dimensions via single-camera in-line digital holography. *N. J. Phys.* 10:125013

Malkiel E, Abras JN, Katz J. 2004. Automated scanning and measurements of particle distributions within a holographic reconstructed volume. *Meas. Sci. Technol.* 15:601–12

Malkiel E, Abras JN, Widder EA, Katz J. 2006. On the spatial distribution and nearest neighbor distance between particles in the water column determined from in situ holographic measurements. *J. Plankton Res.* 28:149–70

Malkiel E, Alquaddoomi O, Katz J. 1999. Measurements of plankton distribution in the ocean using submersible holography. *Meas. Sci. Technol.* 10:1142–52

Malkiel E, Sheng I, Katz J, Strickler JR. 2003. The three-dimensional flow field generated by a feeding calanoid copepod measured using digital holography. *J. Exp. Biol.* 206:3657–66

Mann CJ, Yu LF, Lo CM, Kim MK. 2005. High-resolution quantitative phase-contrast microscopy by digital holography. *Opt. Exp.* 13:8693–98

Marquet P, Rappaz B, Magistretti PJ, Cuche E, Emery Y, et al. 2005. Digital holographic microscopy: a noninvasive contrast imaging technique allowing quantitative visualization of living cells with subwavelength axial accuracy. *Opt. Lett.* 30:468–70

Meng H, Hussain F. 1995. In-line recording and off-axis viewing technique for holographic particle velocimetry. *Appl. Opt.* 34:1827–40

Meng H, Pan G, Pu Y, Woodward SH. 2004. Holographic particle image velocimetry: from film to digital recording. *Meas. Sci. Technol.* 15:673–85

Mico V, Zalevsky Z, Ferreira C, Garcia J. 2008. Superresolution digital holographic microscopy for three-dimensional samples. *Opt. Exp.* 16:19260–70

Milgram JH, Li WC. 2002. Computational reconstruction of images from holograms. *Appl. Opt.* 41:853–64

O'Hern TJ, D'Agostino L, Acosta AJ. 1988. Comparison of holographic and Coulter counter measurements of cavitation nuclei in the ocean. *J. Fluids Eng.* 110:200–7

Onural L, Scott PD. 1987. Digital decoding of in-line holograms. *Opt. Eng.* 26:1124–32

Ooms T, Koek W, Braat J, Westerweel J. 2006. Optimizing Fourier filtering for digital holographic particle image velocimetry. *Meas. Sci. Technol.* 17:304–12

Ooms T, Koek W, Westerweel J. 2008. Digital holographic particle image velocimetry: eliminating a sign-ambiguity error and a bias error from the measured particle field displacement. *Meas. Sci. Technol.* 19:074003

Owen RB, Zozulya AA. 2000. In-line digital holographic sensor for monitoring and characterizing marine particulates. *Opt. Eng.* 39:2187–97

Pan G, Meng H. 2003. Digital holography of particle fields: reconstruction by use of complex amplitude. *Appl. Opt.* 42:827–33

Pfitsch DW, Malkiel E, Takagi Y, Ronzhes Y, King S, et al. 2005. Development of a free drifting submersible digital holographic imaging system. In *OCEANS 2005, Proc. MTS/IEEE*. New York: IEEE

Pfitsch DW, Malkiel E, Takagi Y, Ronzhes Y, King S, et al. 2007. Analysis of in-situ microscopic organism behavior in data acquired using a free drifting submersible holographic imaging system. In *OCEANS 2007, Proc. MTS/IEEE*. New York: IEEE

Pu Y, Meng H. 2000. An advanced off-axis holographic particle image velocimetry (HPIV) system. *Exp. Fluids* 29:184–97

Pu Y, Meng H. 2005. Four-dimensional dynamic flow measurement by holographic particle image velocimetry. *Appl. Opt.* 44:7697–708

Pu Y, Song X, Meng H. 2000. Off-axis holographic particle image velocimetry for diagnosing particulate flows. *Exp. Fluids* 29:S117–28

Robinson SK. 1991. Coherent motions in the turbulent boundary layer. *Annu. Rev. Fluid Mech.* 23:601–39

Roichman Y, Cholis I, Grier DG. 2006. Volumetric imaging of holographic optical traps. *Opt. Exp.* 14:10907–12

Roichman Y, Grier DG. 2006. Projecting extended optical traps with shape-phase holography. *Opt. Lett.* 31:1675–77

Royer H. 1997. Holography and particle image velocimetry. *Meas. Sci. Technol.* 8:1562–72

Salazar J, De Jong J, Cao LJ, Woodward SH, Meng H, Collins LR. 2008. Experimental and numerical investigation of inertial particle clustering in isotropic turbulence. *J. Fluid Mech.* 600:245–56

Satake S, Kunugi T, Sato K, Ito T, Taniguchi J. 2005. Three-dimensional flow tracking in a micro channel with high time resolution using micro digital-holographic particle-tracking velocimetry. *Opt. Rev.* 12:442–44
Satake SI, Kanamori H, Kunugi T, Sato K, Ito T, Yamamoto K. 2007. Parallel computing of a digital hologram and particle searching for microdigital-holographic particle-tracking velocimetry. *Appl. Opt.* 46:538–43
Schnars U, Juptner WPO. 2002. Digital recording and numerical reconstruction of holograms. *Meas. Sci. Technol.* 13:R85–101
Schnars U, Sommer K, Grubert B, Hartmann HJ, Juptner W. 1999. Holographic diagnostics of fluid experiments onboard the International Space Station. *Meas. Sci. Technol.* 10:900–3
Schoppa W, Hussain F. 2002. Coherent structure generation in near-wall turbulence. *J. Fluid Mech.* 453:57–108
Sheng J, Malkiel E, Katz J. 2003. Single beam two-views holographic particle image velocimetry. *Appl. Opt.* 42:235–50
Sheng J, Malkiel E, Katz J. 2006. A digital holographic microscope for measuring three dimensional particle distributions and motions. *Appl. Opt.* 45:3893–901
Sheng J, Malkiel E, Katz J. 2008. Using digital holographic microscopy for simultaneous measurements of three-dimensional near wall velocity and wall shear stress in a turbulent boundary layer. *Exp. Fluids* 45:1023–35
Sheng J, Malkiel E, Katz J. 2009. Buffer layer structures associated with extreme wall stress events in a smooth wall turbulent boundary layer. *J. Fluid Mech.* In press
Sheng J, Malkiel E, Katz J, Adolf J, Belas R, Place AR. 2007. Digital holographic microscopy reveals prey-induced changes in swimming behavior of predatory dinoflagellates. *Proc. Natl. Acad. Sci. USA* 104:17512–17
Silverman BA, Belz RA, Farmer WM. 1964. A laser fog disdrometer. *J. Appl. Meteorol.* 3:792–801
Soria J, Atkinson C. 2008. Towards 3C-3D digital holographic fluid velocity vector field measurement: tomographic digital holographic PIV (tomo-HPIV). *Meas. Sci. Technol.* 19:074002
Stewart GL, Beers JR, Knox C. 1973. Application of holographic techniques to the study of marine plankton in the field and in the laboratory. In *Developments in Laser Technology II*, *SPIE Proc.*, ed. R Wuerker, 41:183–88. Bellingham, WA: SPIE
Sun H, Benzie PW, Burns N, Hendry DC, Player MA, Watson J. 2008. Underwater digital holography for studies of marine plankton. *Philos. Trans. R. Soc. A* 366:1789–806
Sun HY, Hendry DC, Player MA, Watson J. 2007. In situ underwater electronic holographic camera for studies of plankton. *IEEE J. Ocean. Eng.* 32:373–82
Svizher A, Cohen J. 2006. Holographic particle image velocimetry measurements of hairpin vortices in a subcritical air channel flow. *Phys. Fluids* 18:014105
Tao B, Katz J, Meneveau C. 2000. Geometry and scale relationships in high Reynolds number turbulence determined from three-dimensional holographic velocimetry. *Phys. Fluids* 12:941–44
Tao B, Katz J, Meneveau C. 2002. Statistical geometry of subgrid-scale stresses determined from holographic particle image velocimetry measurements. *J. Fluid Mech.* 457:35–78
Thompson BJ. 1974. Holographic particle sizing techniques. *J. Phys. E* 7:781–88
Trolinger JD, Belz RA, Farmer WM. 1969. Holographic techniques for study of dynamic particle fields. *Appl. Opt.* 8:957–61
Van Der Bos F, Tao B, Meneveau C, Katz J. 2002. Effects of small-scale turbulent motions on the filtered velocity gradient tensor as deduced from holographic particle image velocimetry measurements. *Phys. Fluids* 14:2456–74
Vest CM. 1979. *Holographic Interferometry*. New York: Wiley & Sons
Vikram CS. 1992. *Particle Field Holography*. Cambridge, UK: Cambridge Univ. Press
Watson J, Alexander S, Craig G, Hendry DC, Hobson PR, et al. 2001. Simultaneous in-line and off-axis subsea holographic recording of plankton and other marine particles. *Meas. Sci. Technol.* 12:L9–15
Watson J, Hobson PR, Krantz EP, Lampitt RS, Rogerson A. 1995. Holographic mensuration of suspended particles in aquatic systems. *Proc. SPIE* 2577:191–99
Willert CE, Gharib M. 1991. Digital particle image velocimetry. *Exp. Fluids* 10:181–93
Willmarth WW, Tu BJ. 1967. Structure of turbulence in the boundary layer near the wall. *Phys. Fluids* 10:S134–37

Xu W, Jericho MH, Meinertzhagen IA, Kreuzer HJ. 2001. Digital in-line holography for biological applications. *Proc. Natl. Acad. Sci. USA* 98:11301–5

Xu W, Jericho MH, Meinertzhagen IA, Kreuzer HJ. 2002. Digital in-line holography of microspheres. *Appl. Opt.* 41:5367–75

Zhang J, Tao B, Katz J. 1997. Turbulent flow measurement in a square duct with hybrid holographic PIV. *Exp. Fluids* 23:373–81

Annual Review of
Fluid Mechanics

Volume 42, 2010

Contents

Singular Perturbation Theory: A Viscous Flow out of Göttingen
Robert E. O'Malley Jr. 1

Dynamics of Winds and Currents Coupled to Surface Waves
Peter P. Sullivan and James C. McWilliams 19

Fluvial Sedimentary Patterns
G. Seminara 43

Shear Bands in Matter with Granularity
Peter Schall and Martin van Hecke 67

Slip on Superhydrophobic Surfaces
Jonathan P. Rothstein 89

Turbulent Dispersed Multiphase Flow
S. Balachandar and John K. Eaton 111

Turbidity Currents and Their Deposits
Eckart Meiburg and Ben Kneller 135

Measurement of the Velocity Gradient Tensor in Turbulent Flows
James M. Wallace and Petar V. Vukoslavčević 157

Friction Drag Reduction of External Flows with Bubble and Gas Injection
Steven L. Ceccio 183

Wave–Vortex Interactions in Fluids and Superfluids
Oliver Bühler 205

Laminar, Transitional, and Turbulent Flows in Rotor-Stator Cavities
Brian Launder, Sébastien Poncet, and Eric Serre 229

Scale-Dependent Models for Atmospheric Flows
Rupert Klein 249

Spike-Type Compressor Stall Inception, Detection, and Control
C.S. Tan, I. Day, S. Morris, and A. Wadia 275

Airflow and Particle Transport in the Human Respiratory System
C. Kleinstreuer and Z. Zhang 301

Small-Scale Properties of Turbulent Rayleigh-Bénard Convection
Detlef Lohse and Ke-Qing Xia 335

Fluid Dynamics of Urban Atmospheres in Complex Terrain
H.J.S. Fernando 365

Turbulent Plumes in Nature
Andrew W. Woods 391

Fluid Mechanics of Microrheology
Todd M. Squires and Thomas G. Mason 413

Lattice-Boltzmann Method for Complex Flows
Cyrus K. Aidun and Jonathan R. Clausen 439

Wavelet Methods in Computational Fluid Dynamics
Kai Schneider and Oleg V. Vasilyev 473

Dielectric Barrier Discharge Plasma Actuators for Flow Control
Thomas C. Corke, C. Lon Enloe, and Stephen P. Wilkinson 505

Applications of Holography in Fluid Mechanics and Particle Dynamics
Joseph Katz and Jian Sheng 531

Recent Advances in Micro-Particle Image Velocimetry
Steven T. Wereley and Carl D. Meinhart 557

Indexes

Cumulative Index of Contributing Authors, Volumes 1–42 577

Cumulative Index of Chapter Titles, Volumes 1–42 585

Errata

An online log of corrections to *Annual Review of Fluid Mechanics* articles may be found at http://fluid.annualreviews.org/errata.shtml